RSC Advances

PAPER

View Article Online
View Journal | View Issue

Cite this: *RSC Adv.*, 2023, **13**, 28179

Asterarcys quadricellulare algae-mediated copper oxide nanoparticles as a robust and recyclable catalyst for the degradation of noxious dyes from wastewater†

Manisha Khandelwal,[a] Sunita Choudhary,[b] Harish,[b] Ashok Kumawat,[c] Kamakhya Prakash Misra,[c] Devendra Singh Rathore[d] and Rama Kanwar Khangarot*[a]

The present article explores the synthesis of copper oxide nanoparticles (CuO NPs) utilizing *Asterarcys quadricellulare* algal extract and examines the effect of various reaction parameters on the size and morphology of the nanoparticles. The samples were thoroughly characterized using XRD, FTIR, UV-vis, FE-SEM, and EDS techniques. The XRD analysis disclosed that the size of the synthesized nanoparticles could be controlled by adjusting the reaction parameters, ranging from 4.76 nm to 13.70 nm along the highest intensity plane (111). FTIR spectroscopy provided evidence that the phytochemicals are present in the algal extract. We have compared the photocatalytic activity of biologically and chemically synthesized CuO NPs and observed that biologically synthesized CuO NPs showed better photocatalytic activity than chemically synthesized CuO NPs. The biosynthesized CuO NPs (S8) demonstrated outstanding photodegradation activity towards four different organic dyes, namely BBY, BG, EBT, and MG, with degradation percentages of 95.78%, 98.02%, 94.15%, and 96.04%, respectively. The maximum degradation efficacy of 98.02% was observed for the BG dye at optimized reaction conditions and 60 min of visible light exposure. The kinetics of the photodegradation reaction followed the pseudo-first-order kinetic model, and the rate constant (k) was calculated using the Langmuir–Hinshelwood model for each dye. This study provides an efficient and sustainable approach for synthesizing CuO NPs with superior photocatalytic degradation efficiency towards organic dyes.

Received 3rd August 2023
Accepted 15th September 2023

DOI: 10.1039/d3ra05254k

rsc.li/rsc-advances

Introduction

Wastewater treatment is a critical area of research due to its significance in protecting the ecosystem. With the advancement in industrialization and urbanization, the amount of wastewater produced has increased exponentially, leading to the release of harmful pollutants into the ecosystem.[1,2] Organic dyes are widely utilized in the textile,[3] leather,[4] paper,[5] and food industries[6] and have emerged as one of the significant pollutants in wastewater. These dyes pose a substantial threat to the environment as they are non-biodegradable and can persist for a longer time, leading to water pollution and health hazards due to their toxicity, carcinogenicity, and mutagenicity.[7] The commonly used dyes are bismarck brown Y (BBY), brilliant green (BG), eriochrome black T (EBT), malachite green (MG), and so on, which have adverse impacts on the environment. BBY, BG, and MG dyes are used in the dyeing of wool, silk, leather, textile, and paper and also in the preparation of biological stains.[8–10] EBT dye is utilized as a complexometric indicator for metal ions in analytical chemistry.[11] The presence of these organic dyes in wastewater is associated with severe health hazards, including toxicity to aquatic organisms and potential risks to human health, such as respiratory difficulties, skin irritation, and allergies. Consequently, researchers have focused their efforts on developing methods to eliminate these dyes from water sources in order to mitigate their environmental impact.[12] Various chemical and physical methods have been employed to solve the problem, such as coagulation, flocculation, ion exchange, membrane filtration, and adsorption.[13] Although these physiochemical approaches are effective in separating the dyes from wastewater, the toxicity of the dyes from the environment is not eliminated completely. Moreover,

[a]*Department of Chemistry, University College of Science, Mohanlal Sukhadia University, Udaipur-313001, Rajasthan, India. E-mail: ramakanwar@mlsu.ac.in*
[b]*Department of Botany, University College of Science, Mohanlal Sukhadia University, Udaipur-313001, Rajasthan, India*
[c]*Department of Physics, School of Basic Sciences, Manipal University Jaipur, Jaipur-303007, Rajasthan, India*
[d]*Department of Environmental Sciences, Mohanlal Sukhadia University, Udaipur-313001, Rajasthan, India*

† Electronic supplementary information (ESI) available: All experimental details are explained. See DOI: https://doi.org/10.1039/d3ra05254k

these physiochemical methods are costly and ineffective, leading to the generation of secondary byproducts requiring additional processing. Over the last decade, photocatalysis has gained attention as a potential method for the efficient degradation of organic dyes from wastewater.[14,15] This method involves the use of a photocatalyst, typically composed of metal oxide nanoparticles, to facilitate the breakdown of organic pollutants under the influence of light.[16]

Metallic nanomaterials obtained from earth-abundant and inexpensive metals have gained considerable attention owing to their potential as practicable alternatives to rare and expensive metals such as gold,[17] silver,[18,19] platinum,[20] titanium,[21] *etc.* Among many nanomaterials understudy the copper oxide nanoparticles (CuO NPs) have gained considerable attention due to their desirable physical and chemical properties, including catalytic, optical, electrical, and magnetic properties.[22,23] Additionally, having a high surface area to volume ratio, CuO NPs exhibit antibacterial and biocidal properties and are effective in reducing organic pollutants like organic dyes, heavy metals, phenols, nitrogen-containing fertilizers, insecticides, and other agrochemicals.[24,25] As a result, researchers have identified CuO NPs as a viable solution for removing organic dyes from wastewater.

Several methods have been developed for the synthesis of CuO NPs, including chemical, physical, and biological approaches. Among these, the biological method is green, reliable, eco-friendly, cost-effective, and novel for the synthesis of CuO NPs.[26] The biogenic route of copper-based nanomaterials synthesis includes utilization of plant extracts, *viz.*, root, bark, stem, leaf, flower, fruit, and seed and also microorganisms, for example, algae, bacteria, yeast, virus, and fungi.[27] Especially, the use of algae for synthesizing CuO NPs has yet to be extensively studied. Algae contain several bioactive compounds, such as polysaccharides, proteins, and enzymes, that aid in the reduction and stabilization of metal ions, resulting in the synthesis of nanoparticles with high purity and yield.[28] Moreover, algal extract offers superior control over the shape and size of the synthesized nanoparticles. Therefore, the algal extract-mediated synthesis of nanoparticles is a promising and sustainable approach for the green synthesis of nanoparticles with potential applications in various fields such as medicine, energy, and environmental remediation.[29] There are only a few reports published on the synthesis of CuO NPs using algal extract. In 2014, Abboud *et al.* synthesized highly stable CuO NPs by utilizing brown algae *Bifurcaria bifurcate* and studied their antibacterial activity against two different strains of bacteria *Staphylococcus aureus* and *Enterobacter aerogenes*.[30] Ramaswamy *et al.* reported the synthesis of CuO NPs using brown algae (*Sargassum polycystum*) mediated the synthesis of CuO NPs. The synthesized CuO NPs showed good anticancer activity against breast MCF-7 cells.[31] Parsaee and co-workers studied the biosynthesis of CuO NPs *via* ultrasound method utilizing the *Cystoseira trinodis* algal extract as an eco-friendly and time-saving process. The synthesized NPs were used to study the photocatalytic degradation of methylene blue (MB) dye.[32] Banerjee and co-authors synthesized CuO NPs using *Anabaena cylindrica* algae extract. The also investigated the influence of the concentration of algal extract, pH, stirring speed, and Cu^{2+} ions concentration on the size and shape of CuO NPs.[33] Simultaneously, Rubilar and colleagues studied the synthesis of CuO NPs using protein fraction of brown algae *Macrocystis pyrifera*.[34] In 2021, Kumar *et al.* reported the *Sargassum longifolium* algal extract mediated synthesis of CuO NPs and studied their antioxidant and antibacterial properties.[35] However, the synthesis of CuO NPs using the *Asterarcys quadricellulare* is hitherto unreported.

Therefore, the present work aims to explore the synthesis of CuO NPs utilizing *Asterarcys quadricellulare* algal extract. The effect of various reaction parameters, such as pH, reaction time, the volume of algal extract, and the concentration of copper ions on the size and morphology of CuO NPs were also examined. The synthesized nanoparticles were characterized by different techniques, including XRD, FTIR, UV-vis, and FE-SEM coupled with EDS. Additionally, we have investigated the efficiency of the synthesized CuO NPs in the photocatalytic degradation of commonly used organic dyes, such as BBY, BG, EBT, and MG.

The significance of this research lies in its ability to simultaneously address two major environmental challenges. By employing a green approach for the synthesis of CuO NPs, we have followed the principles of green chemistry, which are essential for a sustainable environment and human health. Algae can have harmful effects on the environment and human health when they grow uncontrollably. Algal blooms can deplete oxygen in the water, create toxins that can harm humans and animals, and upset the natural balance of aquatic ecosystems. Additionally, algal blooms can have a negative economic impact on the fishing and tourism industries and can attach themselves to boats and other structures, causing fouling and damage. Therefore, using algae as a source of nanoparticle synthesis shall help to maintain the balance in the ecosystem by reducing the levels of algae in the environment and mitigating the adverse effects of algae. Furthermore, the elimination of organic dyes, *i.e.*, BBY, BG, EBT, and MG, using the algal-mediated CuO NPs cleans the water bodies by removing noxious dyes from the wastewater. Overall, the research presented here is potentially transformative, offering dual benefits for environmental remediation and sustainability.

Experimental section

The materials and methods used for the synthesis of CuO NPs and photocatalytic experiments are discussed in detail in the ESI.† The algal-mediated CuO NPs were synthesized by varying single parameter and keeping other parameters constant. The entire manuscript contains some notations for the convenience of the readers. The sample names S1, S2, and S3 were used to denote the synthesized CuO NPs at pH 10, 11, and 12, respectively. The sample names S2, S4, and S5 were used to depict the synthesized CuO NPs at varying reaction time 24 h, 48 h, and 72 h, respectively. The synthesized CuO NPs at the different volumes of algal extract were designated as S6, S2, and S7 for the 5 mL, 10 mL, and 15 mL algal extract volumes, respectively. The S8, S9, and S10 sample names were utilized to denote the

synthesized CuO NPs at different concentrations of the copper ions 0.05 M, 0.1 M, and 0.2 M, respectively. Lastly, the S11 sample name was used to represent the chemically synthesized CuO NPs.

Results and discussion

Optimization of the biosynthesis of CuO NPs

The impact of the various parameters on the *Asterarcys quadricellulare* algal extract-mediated green synthesis of CuO NPs was investigated. These parameters were found to be significant in controlling the size and morphology of the biosynthesized CuO NPs. The parameters include the effect of pH, reaction time, the volume of algal extract, and the concentration of copper ions, which will be elaborated upon in the subsequent sections.

pH. The size and shape of the synthesized CuO NPs are strongly influenced by the pH at which they were synthesized. Upon reviewing the existing literature, it was determined that the synthesis of CuO NPs exhibited favourable outcomes under alkaline pH conditions.[33,36] Thus, pH values of 10, 11, and 12 were selected to synthesize the CuO NPs (Table 1). The XRD analysis along the highest intensity plane (111) disclosed that the sizes of CuO NPs were 8.61, 8.05, and 9.41 nm at pH 10, 11, and 12, respectively. The nanoparticle synthesized at pH 11 exhibited the smallest size compared to those produced at pH 10 and 12. Therefore, for subsequent investigations, pH 11 was chosen as the optimal pH for the biosynthesis of the CuO NPs.

Time. Table 2 shows the reaction conditions of an investigation of the impact of time on the biosynthesis of CuO NPs. The findings indicate that the size and morphology of the nanoparticles were significantly influenced by the reaction time. Specifically, an increase in reaction time from 24 h to 72 h led to an increase in the size of CuO nanoparticles from 8.05 to 13.70 nm, along the highest intensity plane (111). The longer reaction time resulted in a larger crystallite size due to the formation of agglomerates. Therefore, 24 h was selected as the optimal reaction time for the synthesis of CuO NPs.

The volume of algal extract. The effect of the volume of *Asterarcys quadricellulare* algal extract on the biosynthesis of CuO NPs was studied, as shown in Table 3. The highest intensity plane (111) of the XRD pattern was used as the basis of crystallite size analysis. The XRD results indicate that the crystallite size of the CuO NPs synthesized by 5 mL of algal extract was 7.34 nm. However, when the volume of the algal extract was enhanced to 10 mL and 15 mL, the crystallite size increased to 8.05 nm and 8.49 nm, respectively. Based on these findings, it was concluded that 5 mL of *Asterarcys quadricellulare* algal extract was the optimum volume to synthesize CuO NPs.

The concentration of copper ions. To investigate the influence of copper ion concentration on the biosynthesis of CuO NPs, the concentration was varied from 0.05 M to 0.2 M (Table 4). The XRD analysis disclosed that the sizes of the CuO NPs obtained at copper ions concentrations of 0.05 M, 0.1 M, and 0.2 M were found to be 4.73, 6.65, and 7.62 nm, respectively, along the highest intensity XRD plane (111). The observed results can be attributed to the fact that increasing the concentration of copper ions results in higher availability of copper ions for reduction and nucleation. This leads to a higher rate of nanoparticle growth, resulting in a larger crystallite size. In the present study, it was observed that lowering the concentration of copper ions led to a decrease in the crystallite size of the synthesized CuO NPs. Although, the lower concentration of copper ions resulted in an insufficient amount of CuO NPs. Therefore, we selected a higher concentration (0.2 M) to optimize other reaction parameters for the biosynthesis of CuO NPs.

Proposed mechanism for *Asterarcys quadricellulare* algal-mediated green synthesis of CuO NPs

The synthesis of CuO NPs using *Asterarcys quadricellulare* algae proceeded *via* two steps, *i.e.*, reduction and oxidation, through the action of algal biomass or its metabolites such as carbohydrates, proteins, enzymes, and lipids. In the first step, metabolites function as a reducing agent and transform the Cu^{2+} ions to Cu^{0}. In the second step, the Cu^{0} formed in the first step undergo oxidation to form CuO NPs. The oxidation process was initiated by the dissolved oxygen present in the reaction medium. The subsequent crystal growth continued until the CuO NPs attained a stable size and morphology.[37,38] The metabolites also act as a capping and stabilizing agent in the agglomeration of CuO NPs. The plausible mechanism of CuO NPs synthesis using *Asterarcys quadricellulare* algae is illustrated in Fig. 1.

Characterization techniques

XRD analysis. The XRD patterns of all the synthesized CuO NPs are represented in Fig. 2. The diffraction peak located around 2θ values of 32.43°, 35.50°, 38.77°, 48.72°, 53.28°, 58.26°, 61.53°, 66.16°, and 68.21° corresponding to the (110), ($\bar{1}$11), (111), ($\bar{2}$02), (020), (202), ($\bar{1}$13), ($\bar{3}$11), and (220) planes, respectively. The XRD peaks were well indexed with the standard JCPDS card no. 80-1916 (Fig. 2a).[39] These results indicate that the CuO NPs have a polycrystalline nature, monoclinic structure, and end-centered lattice.

Table 1 Conditions of synthesis of CuO NPs samples by variation of pH values

S. no.	Sample name	pH	Time	Volume of algal extract	Concentration of copper ions	Temperature	Size of CuO NPs
1	S1	10	24 h	10 mL	0.2 M	60 °C	8.61 nm
2	S2	11	24 h	10 mL	0.2 M	60 °C	8.05 nm
3	S3	12	24 h	10 mL	0.2 M	60 °C	9.41 nm

Table 2 Conditions of synthesis of CuO NPs samples by variation of reaction time

S. no.	Sample name	Time	pH	Volume of algal extract	Concentration of copper ions	Temperature	Size of CuO NPs
1	S2	24 h	11	10 mL	0.2 M	60 °C	8.05 nm
2	S4	48 h	11	10 mL	0.2 M	60 °C	11.64 nm
3	S5	72 h	11	10 mL	0.2 M	60 °C	13.70 nm

No additional peak was observed in all samples, which indicated that the synthesized CuO NPs were phase pure.

Upon conducting a thorough analysis of the major XRD peaks, it was observed that there was a slight shift in the 2θ values on a variation of the reaction parameters. Fig. S1† displays a plot of the diffraction angles corresponding to prominent peaks of $(\bar{1}11)$ and (111) planes against the sample names. The influence of pH, reaction time, algal extract volume, and copper salt ions concentration on the 2θ values was observed. The analysis showed that the 2θ values initially decreased when the pH increased from 10 to 11, and then the 2θ values increased as the pH reached 12. An increase in the reaction time resulted in elevated 2θ values along both major crystallographic planes $(\bar{1}11)$ and (111). This could be attributed to the growth of the crystal lattice structure with prolonged reaction time. Furthermore, with the enhancement of algal extract volume, the 2θ values decreased along $(\bar{1}11)$ plane and increased along (111) plane. It was observed that an increase in Cu^{2+} ions concentration resulted in an increase in the 2θ values along the $(\bar{1}11)$. However, for the (111) plane, the 2θ values first decreased and then increased with increasing Cu^{2+} ions concentration.

Orientation parameter. For each sample, the orientation parameter ($\gamma_{(hkl)}$) corresponding to a particular plane with Miller indices (hkl) is determined by eqn (1).[40]

$$\gamma_{(hkl)} = \frac{I_{(hkl)}}{I_{(110)} + I_{(\bar{1}11)} + I_{(111)} + I_{(\bar{2}02)} + I_{(020)} + I_{(202)} + I_{(\bar{1}13)} + I_{(\bar{3}11)} + I_{(220)}} \quad (1)$$

The intensities of crystallographic planes with Miller indices (hkl) are denoted by $I_{(hkl)}$, and their corresponding $\gamma_{(hkl)}$ values are listed in Table 5. The increase in the pH value degraded the crystal growth of CuO NPs along the (110) plane and improved it along the (111) plane, as indicated by $\gamma_{(hkl)}$ values. The $\gamma_{(hkl)}$ values with an increase in the reaction time enhanced along the (111) plane and degrade along the (110) plane. With the increase in the algal extract volume the crystal growth reduced along the (111) plane. The random variation of $\gamma_{(hkl)}$ along other crystallographic planes and factors indicated the random growth and distribution of particles.

Crystallite size. The full width at half maximum (FWHM, β) of the provided peak, Bragg diffraction analogous to the diffraction peak (θ), and wavelength (λ) of X-rays were used to estimate the crystallite size (t_S) of the nanoparticles using the Scherrer eqn (2).[41]

$$t_s = \frac{k\lambda}{\beta \cos \theta} \quad (2)$$

where k is a constant having value of approximately 1. Table 6 represents the calculated values of crystallite size of CuO NPs under different reaction conditions. The data indicated that all synthesized CuO NPs were nanocrystalline, with crystallite sizes ranging from 1.88 to 25.58 nm. Among all the biosynthesized CuO NPs, the lowest crystallite size 4.73 nm was shown by the S8 sample (reaction condition: pH – 11, time – 24 h, algal extract volume – 5 mL, and copper ions concentration – 0.05 M) along the highest intensity plane (111). While chemically synthesized CuO NPs (S11) had the highest crystallite size of 17.68 nm corresponding to the same plane.

Dislocation density. XRD is an indirect method of calculating the dislocation density. It is a measure of the number of dislocations in a unit volume of a crystalline material and gives information from a macroscopic area in a statistically averaged manner. Using eqn (3), the dislocation density ($\delta_{(hkl)}$) of all synthesized CuO NPs along each plane (hkl) was calculated and shown in Table 7.

$$\delta_{(hkl)} = \frac{1}{(t_s)^2} \quad (3)$$

There is no definite trend of the variation of ($\delta_{(hkl)}$) along any crystallographic plane.

W–H analysis of crystallite size and lattice strain. Qualitative peak profile analysis is often conducted using the W–H plot as it overlooks various factors. It does not take into account various factors, which are domain shape, profile size (Lorentzian or

Table 3 Conditions of synthesis of CuO NPs samples by variation of the volume of algal extract

S. no.	Sample name	Volume of algal extract	pH	Time	Concentration of copper ions	Temperature	Size of CuO NPs
1	S6	5 mL	11	24 h	0.2 M	60 °C	7.34 nm
2	S2	10 mL	11	24 h	0.2 M	60 °C	8.05 nm
3	S7	15 mL	11	24 h	0.2 M	60 °C	8.49 nm

Table 4 Conditions of synthesis of CuO NPs samples by variation of the concentrations of copper ions

S. no.	Sample name	Concentration of copper ions	pH	Time	Volume of algal extract	Temperature	Size of CuO NPs
1	S8	0.05 M	11	24 h	5 mL	60 °C	4.73 nm
2	S9	0.1 M	11	24 h	5 mL	60 °C	6.65 nm
3	S10	0.2 M	11	24 h	5 mL	60 °C	7.62 nm

Gaussian), elastic anisotropy, and the real source of the microstrain, *etc.* The W–H plot was utilized to make an approximate assessment of the influence of strain on the crystallite size. Using the XRD patterns of synthesized CuO NPs, a graph was plotted with $\beta \cos \theta$ on the y-axis and $\sin \theta$ on the x-axis, and a linear fit was applied to the curve to compare it with the given eqn (4) (ref. 42) (Fig. S2†).

$$\beta \cos \theta = \frac{C\lambda}{(t_{WH})} + 2\varepsilon \sin \theta \quad (4)$$

The equation of the trend-line fit, along with the regression factor (R^2), was presented in the inset of the W–H plot for each sample in Fig. S2.† However, it should be noted that the W–H plot is known to neglect several factors, which can result in poor goodness of fit. This is evident from the data points being far away from the trend-line fit, and the uncertainties being represented by the standard error bars. As a result, lower values of the regression factors were observed for all the samples. The constant C was taken as 0.9, and the correction factor was used in the equation to account for any deviations from the ideal model. Overall, the W–H plot provides an approximate evaluation of the impact of strain on crystallite size, but the results should be interpreted with caution due to the limitations of the method.

The average crystallite size (t_{WH}) and the microstrain obtained by performing the W–H plot are already listed in Table 6. The initial two samples (S1–S2) show the compressive strain, and thereafter (S3–S11), its nature changes to tensile. It was noticed that the higher microstrain caused a larger difference between the crystallite sizes obtained by two methods (t_S and t_{WH}). The strongest intensity peak, *i.e.*, (111), was taken to compare both crystallite sizes. The sample with the lowest amount of microstrain had close values of t_S and t_{WH}, and that with the largest one had farther t_S and t_{WH}.

FTIR spectra. FTIR spectra were recorded to identify major functional groups present in the metabolites of *Asterarcys quadricellulare* algae and CuO NPs (Fig. 3). The FTIR spectra of *Asterarcys quadricellulare* algae and all the samples (S1 to S10) except S11 showed distinctive bands at 3848, 3615, 3743, 3652, 2369, 2327, 1689, 1532, 1034, and 873 cm^{-1}. The band at 3848, 3743, 3615, and 3652 cm^{-1} ascribed to the O–H stretching vibrations of moisture, alcohol, phenols, and N–H stretching vibrations of the amide group present in the proteins of algae.[43,44] The band at 2369 and 2327 cm^{-1} corresponded to the CO_2 adsorbed on the surface of the nanoparticles.[45,46] The peak at 1689 cm^{-1} is a characteristic peak of N–H bending vibrations in the amide of protein which acts as a capping agent.[47] The strong band at 1532 cm^{-1} exhibited the presence of the symmetric stretching of the carboxyl group (COO^-) present in the acid residue of the protein molecule.[48,49] The peak at 1034 cm^{-1} indicated the existence of C–O stretching vibrations or C–H bending vibrations of carbohydrates (glucose residue by

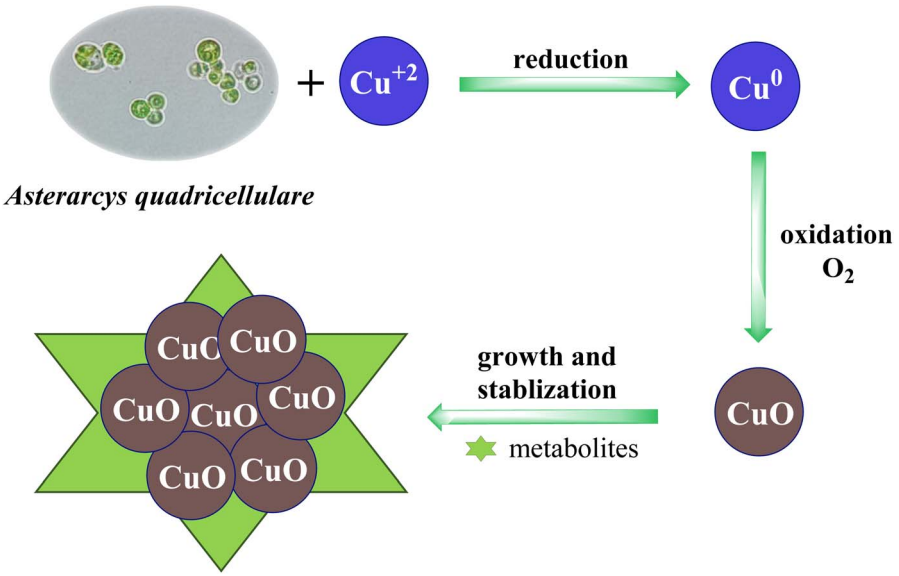

Fig. 1 A plausible mechanism of CuO NPs synthesis using *Asterarcys quadricellulare* extract.

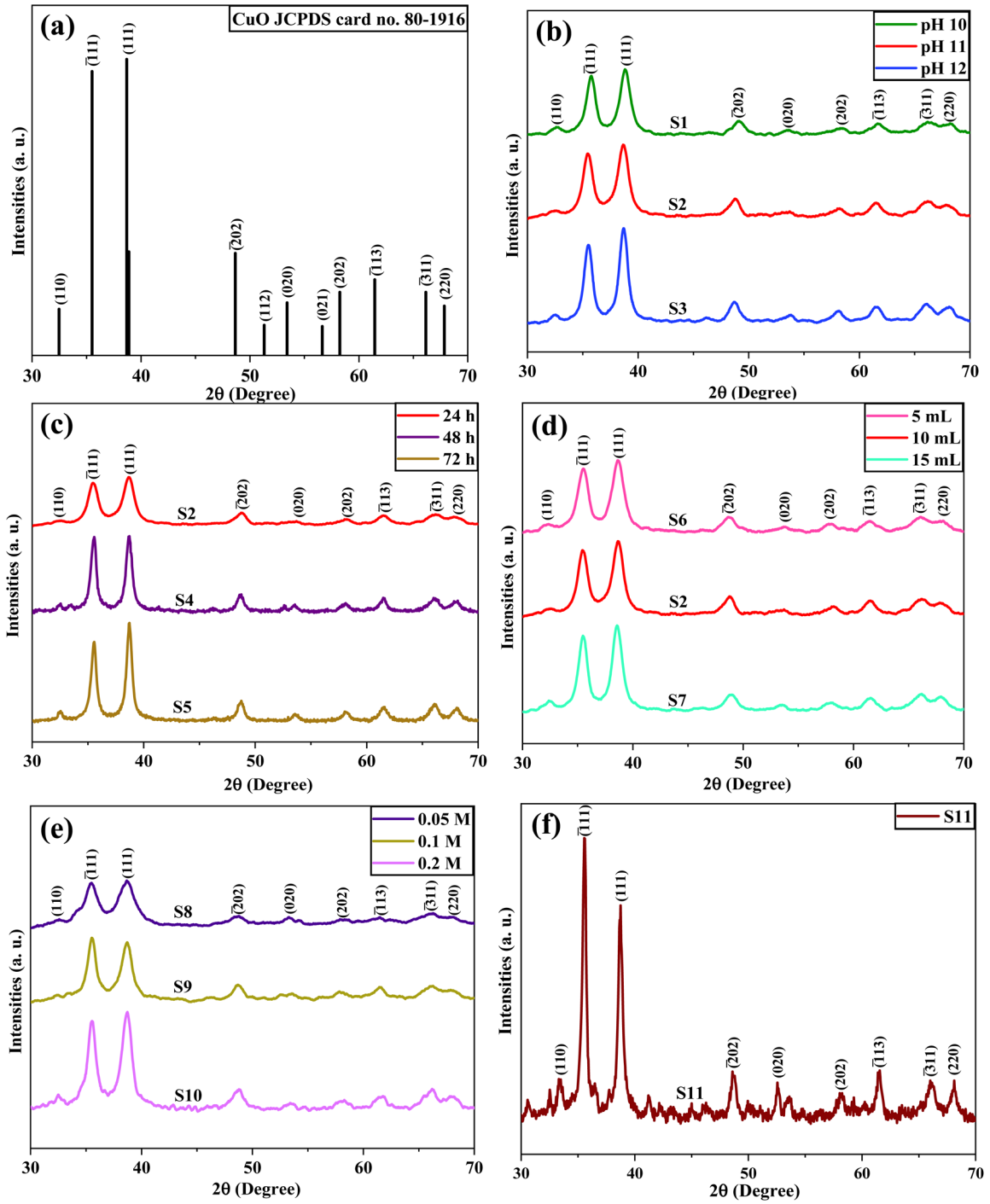

Fig. 2 (a) The standard JCPDS card of CuO NPs, (b) effect of pH of the solution (S1 – pH 10, S2 – pH 11, S3 – pH 12), (c) effect of reaction time (S2 – 24 h, S4 – 48 h, S5 – 72 h), (d) effect of the volume of algal extract (S6 – 5 mL, S2 – 10 mL, S7 – 15 mL), and (e) effect of copper ions concentration (S8 – 0.05 M, S9 – 0.1 M, S10 –0.2 M), on the XRD patterns of biosynthesized CuO NPs; (f) XRD pattern of chemically synthesized CuO NPs (S11).

C–OH bond).[43,50] The band at 873 cm^{-1} denoted C–H bending due to aromatic groups.[51]

The samples S1 to S11 show additional characteristic peaks at 603 and 522 cm^{-1}. The peaks at 603 and 522 cm^{-1} were associated with the Cu–O stretching vibrations, matching with B_{2u} mode.[52,53] The peaks observed in the spectrum of algae can also be seen in the spectra of biosynthesized CuO NPs. This suggests that proteins, polysaccharides, amides, and long-chain fatty acids are the metabolites responsible for reducing, capping, and stabilizing biosynthesized CuO NPs.

The chemically synthesized CuO NPs represented by S11 showed peaks at 3576, 1113, 603, and 524 cm^{-1}. The small

Table 5 Orientation parameters along distinct crystallographic planes

	Orientation parameters ($\gamma_{(hkl)}$)								
Sample name	(110)	($\bar{1}$11)	(111)	($\bar{2}$02)	(020)	(202)	($\bar{1}$13)	($\bar{3}$11)	(220)
S1	0.0799	0.1888	0.2166	0.0955	0.0751	0.0789	0.0853	0.0933	0.0864
S2	0.0677	0.2000	0.2310	0.0956	0.0640	0.0764	0.0882	0.0901	0.0863
S3	0.0618	0.2175	0.2501	0.0878	0.0640	0.0740	0.0806	0.0844	0.0795
S4	0.0557	0.2675	0.2700	0.0848	0.0525	0.0569	0.0739	0.0738	0.0647
S5	0.0524	0.2565	0.3129	0.0829	0.0439	0.0509	0.0647	0.0734	0.0621
S6	0.0775	0.2146	0.2351	0.0865	0.0673	0.0698	0.0839	0.0865	0.0788
S7	0.0806	0.2015	0.2107	0.0857	0.0775	0.0725	0.0837	0.1005	0.0872
S8	0.0809	0.1785	0.1985	0.0934	0.0917	0.0826	0.0867	0.0992	0.0884
S9	0.0745	0.2192	0.1948	0.0952	0.0738	0.0767	0.0945	0.0886	0.0826
S10	0.0857	0.2013	0.1994	0.0964	0.0727	0.0788	0.0860	0.0947	0.0848
S11	0.0745	0.2677	0.2133	0.0824	0.0722	0.0620	0.0824	0.0716	0.0734

hump at 3576 cm^{-1} and 1113 cm^{-1} were ascribed to O–H stretching and O–H bending vibrations, respectively. These peaks were observed due to water molecules adsorbed at the surface of the nanoparticles. The prominent peaks at 603 and 524 cm^{-1} manifested the presence of Cu–O stretching vibrations.[52]

Tauc plot. The UV-visible spectra of CuO NPs were analyzed to determine the band gap value. The band gap of synthesized nanoparticles was estimated by Tauc plot which is represented in Fig. 4. The band gap refers to the energy difference between the valence band (VB) and the conduction band (CB) of a material. It determines the ability of the material to absorb and emit light and therefore plays a crucial role in its optical and electronic properties. The band gap value is yielded by extrapolating the linear region of the curve $[(\alpha h\nu)^2$ *vs.* $h\nu]$ to the *x*-axis.[54,55] The variation in the physiochemical parameter also changes the band gap value of the synthesized CuO NPs. At pH 10, 11, and 12, the observed band gap values were 1.82, 2.30, and 2.06 eV, respectively. The results indicated that the material's band gap was highest at pH 11. Increasing the reaction time from 24 h to 48 h resulted in a decrease in the band gap value from 2.30 to 2.20 eV. This suggests that longer reaction time produce larger nanoparticles with lower band gap values, while shorter reaction time produce smaller nanoparticles with a larger band gap. The volume of algal extract used in the synthesis reaction was also found to affect the band gap value. The band gap values for 5 mL, 10 mL, and 15 mL of algal extract were 2.56, 2.30, and 2.18 eV, respectively. Increasing the algal extract volume resulted in larger nanoparticles with lower band gap values. The same behaviour was observed with the concentration of copper salt ions, where an increase in concentration resulted in a decrease in the band gap value from 2.93 to 2.29 eV. Overall, controlling the reaction parameters, such as pH, reaction time, the algal extract volume, and the copper ions concentration to biosynthesize CuO NPs can be used to tune the band gap of the material. This optimization can help to improve the efficacy of nanoparticles in diverse applications such as solar energy conversion, photocatalysis, and electronic devices. The observed band gap of chemically synthesized CuO NPs was 3.22 eV. In view of the application of photocatalytic activity, the band gap value is a crucial factor to consider. Based on this, it can be inferred that the S8 sample, which has a band gap value of 2.93 eV, is anticipated to exhibit the highest photocatalytic activity among the synthesized CuO NPs.

FE-SEM and EDS analysis. The FE-SEM images of the synthesized CuO NPs are depicted in Fig. 5. The observed surface area (length × width) of CuO NPs while scanning FE-

Table 6 Strain and crystallite size were evaluated by the Scherrer equation and W–H plot along various crystallographic planes

	Crystallite size (t_S) (nm)										
Sample name	(110)	($\bar{1}$11)	(111)	($\bar{2}$02)	(020)	(202)	($\bar{1}$13)	($\bar{3}$11)	(220)	t_{WH}	Microstrain (ε)
S1	6.12	8.59	8.61	6.38	28.51	25.58	7.62	7.66	9.16	6.00	−0.0089
S2	4.46	7.24	8.05	6.25	4.73	10.88	9.48	4.14	18.40	4.51	−0.0114
S3	5.55	9.51	9.41	6.56	8.29	6.43	6.77	5.34	9.51	13.07	0.0118
S4	3.05	12.43	11.64	6.95	1.88	2.64	6.17	4.86	4.46	8.66	0.0196
S5	4.33	13.18	13.70	8.92	4.30	4.34	6.16	6.88	5.37	12.48	0.0130
S6	7.20	7.11	7.34	5.12	3.84	8.04	3.77	16.59	7.20	8.35	0.0074
S7	7.14	9.11	8.49	5.24	11.46	4.37	5.24	11.35	4.26	16.70	0.0151
S8	5.52	6.18	4.73	2.85	6.56	2.74	3.38	4.07	4.71	8.77	0.0206
S9	12.58	10.33	6.65	7.13	5.16	2.56	8.00	3.79	9.60	13.86	0.0288
S10	7.59	9.50	7.62	6.90	13.54	11.98	9.10	5.81	8.04	8.83	0.0010
S11	17.16	20.48	17.68	14.46	19.07	11.08	13.53	9.66	12.43	86.62	0.0095

Table 7 Dislocation density ($\delta_{(hkl)}$) along different crystallographic planes

	$\delta_{(hkl)} \times 10^{15}$ m^{-2}								
Sample name	(110)	($\bar{1}$11)	(111)	($\bar{2}$02)	(020)	(202)	($\bar{1}$13)	($\bar{3}$11)	(220)
S1	0.0267	0.0135	0.0135	0.0246	0.0012	0.0015	0.0172	0.0170	0.0119
S2	0.0503	0.0191	0.0154	0.0256	0.0447	0.0084	0.0111	0.0583	0.0029
S3	0.0325	0.0110	0.0113	0.0232	0.0145	0.0242	0.0218	0.0351	0.0111
S4	0.1075	0.0065	0.0074	0.0207	0.2829	0.1435	0.0263	0.0423	0.0503
S5	0.0533	0.0057	0.0053	0.0126	0.0541	0.0531	0.0263	0.0211	0.0347
S6	0.0192	0.0198	0.0186	0.0381	0.0678	0.0155	0.0704	0.0036	0.0193
S7	0.0196	0.0120	0.0139	0.0364	0.0076	0.0524	0.0364	0.0078	0.0551
S8	0.0328	0.0262	0.0447	0.1231	0.0232	0.1332	0.0875	0.0604	0.0451
S9	0.0063	0.0094	0.0226	0.0197	0.0375	0.1526	0.0156	0.0697	0.0108
S10	0.0173	0.0111	0.0172	0.0210	0.0054	0.0070	0.0121	0.0296	0.0155
S11	0.0034	0.0024	0.0032	0.0048	0.0027	0.0081	0.0055	0.0107	0.0065

SEM images were 93.21 nm × 33.95 nm, 54.99 nm × 20.44 nm, 49.87 nm × 19.86 nm, 83.00 nm × 44.59 nm, 99.53 nm × 66.79 nm, 109.52 nm × 43.17 nm, 115.65 nm × 89.16 nm, 70.87 nm × 46.44 nm, 73.59 nm × 30.33 nm, 62.82 nm × 19.77 nm, and 110.01 nm × 33.98 nm for the samples S1, S2, S3, S4, S5, S6, S7, S8, S9, S10, and S11, respectively. The method of synthesis, for instance, biological and chemical, also changes the morphology of the synthesized nanoparticles. When we analyzed the effect of pH (S1 – pH 10, S2 – pH 11, S3 – pH 12), the reaction time (S2 – 24 h, S4 – 48 h, S5 – 72 h), the algal extract volume (S6 – 5 mL, S2 – 10 mL, S7 – 15 mL), and the concentration of copper ions (S8 – 0.05 M, S9 – 0.1 M, S10 – 0.2 M) on the biologically synthesized CuO NPs, it was found that all four parameters impacted the growth of nanoparticles in terms of the shape. Prominently, flower petals or the flattened rice structure were visible in the FESEM images. The highest pH (S3) leads to denser petal structures with mostly having vertical orientations. The longest reaction time attempted to convert the petals into cotton ball outgrowths (S5). The largest amount of algal extract evolved the clubbing of petals taking the shape of flowers (S7). The increased concentration of copper ions decreased the cotton ball outgrowths and increased the denser petals structure (S8 to S10). Chemically synthesized CuO NPs (S11) have flat structures with occasional rod-like formations. Hence, it is pertinent to conclude that algal extract mediation can impact the nucleation of CuO NPs, which subsequently can play a significant role in shaping it. It is well established that shape and size both impact the functionalities of the nanoparticles. Apart from the algal extract, the pH, reaction time, and copper ions concentration are also seen to influence the shape of the nanoparticles.

The EDS spectra of all the synthesized CuO NPs are represented in Fig. 6. The spectra showed the characteristic peaks of copper (Cu) and oxygen (O) elements, indicating the presence of CuO NPs. The Cu peak was detected at around 8 keV, while the O peak was observed at around 0.5 keV. The spectrum analysis of some samples revealed the presence of minor peaks that corresponded to sulfur (S) and carbon (C), which are likely attributed to the phytochemicals found in the algal extract coated on the nanoparticles.

Photocatalytic degradation of BBY, BG, EBT, and MG organic dyes

This study examined the photocatalytic activity of synthesized CuO NPs for the degradation of organic dyes such as BBY, BG, EBT, and MG under visible light illumination. The structures of all four dyes are shown in Fig. S3.† The degradation of BBY, BG, EBT, and MG dyes were analyzed using UV-visible spectrophotometer at maximum absorbance wavelength peaks of 450 nm,[8] 624 nm,[56] 548 nm,[57] and 617 nm,[58] respectively. We performed the three sets of experiments, adsorption (in the dark with a catalyst), photolysis (in the light without the catalyst), and photocatalysis (in the light with the catalyst), for all the selected dyes and each sample of CuO NPs (S1–S11). In the two sets, *i.e.*, adsorption and photolysis, very less dye degradation was noticed. While in the case of photocatalysis, significant degradation of dyes was observed (Fig. S4†). The biosynthesized CuO NPs were more efficient than the chemically synthesized CuO NPs for the dilapidation of the dyes. The biosynthesized CuO NPs, S8, exhibited the highest photocatalytic activity, while chemically synthesized CuO NPs, S11, showed the lowest photocatalytic activity. Therefore, in this paper, we have disclosed the results of the S8 sample of CuO NPs only. The effect of various reaction parameters, such as pH, catalyst dosage, and initial dye concentration, on the degradation of all the selected four dyes using biosynthesized CuO NPs (S8) were examined to determine the optimal condition for the dye degradation.

Effect of reaction parameters on photocatalytic activity of BBY, BG, EBT, and MG dyes

Effect of pH. The pH of the solution significantly affects the catalytic efficiency of the catalyst because it alters the stability, colour intensity, and decomposition of the dye. The impact of the solution pH on the photocatalytic activity towards BBY, BG, EBT, and MG dyes was studied, keeping other parameters constant (Fig. S5†). The degradation percentage of BBY dye was decreased with an increase in the pH value (Fig. S5a†). At pH values 3, 5, 7, 9, and 11, the observed degradation percentage was 88.48%, 84.68%, 80.17%, 74.66%, and 62.21%, respectively. The results showed that the maximum degradation of BBY dye occurred at pH 3.

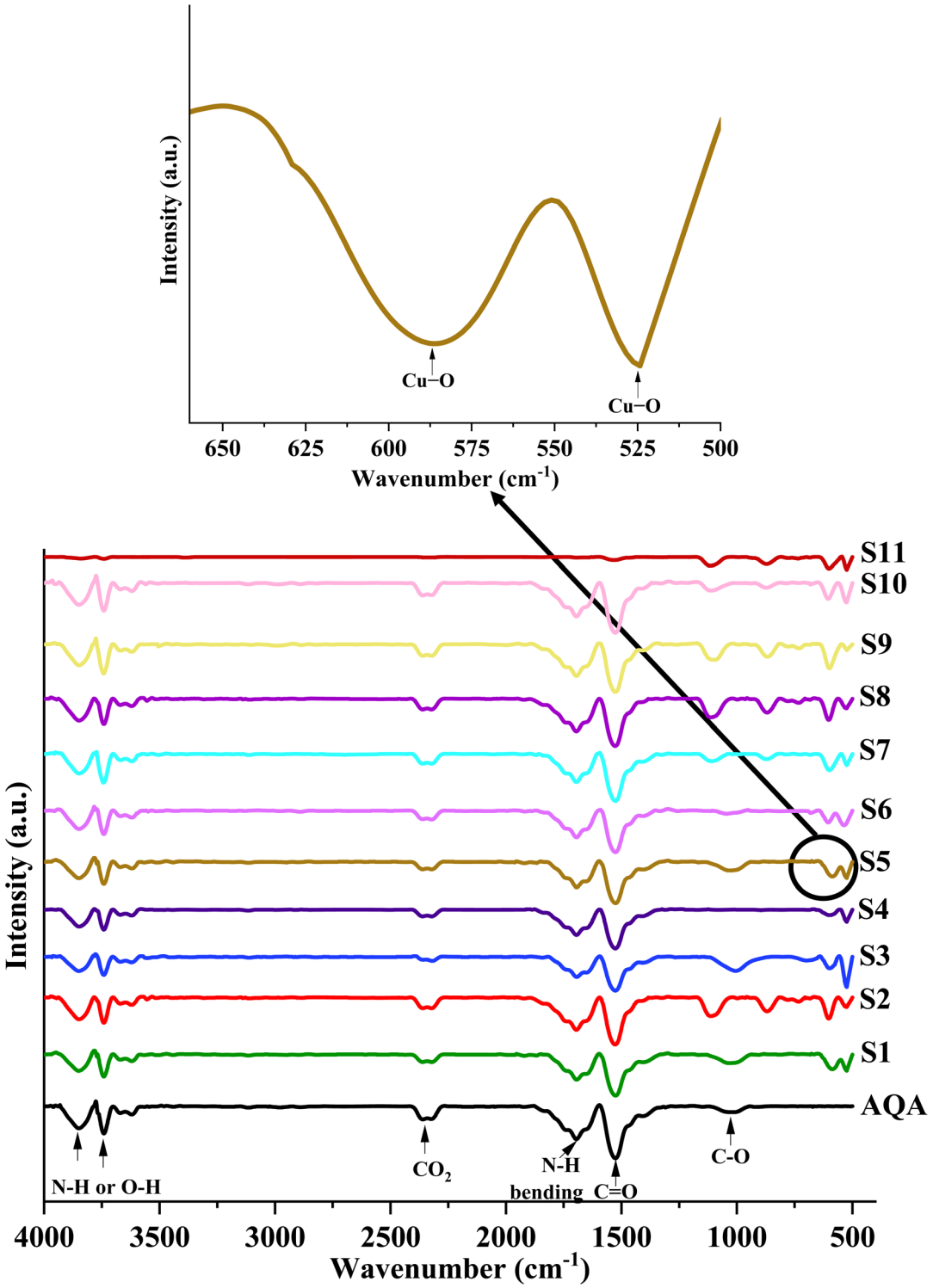

Fig. 3 FTIR spectra of the *Asterarcys quadricellulare* algae (AQA), biosynthesized CuO NPs (S1–S10) and chemically synthesized CuO NPs (S11). The particular segment of the curve is magnified to highlight the presence of copper-oxygen bonds present in all the samples of CuO NPs.

From Fig. S5b,† it was observed that the degradation efficiency of BG dye was increased with an increase in the pH values. The photodegradation rate was enhanced from 58.88% to 85.20% as pH was increased from 3 to 9. With a further increase in pH value to 11, the colour of the dye disappears abruptly within 1 min. At pH 11, the central carbon atom of the BG dye molecule acquired electrophilic nature and is suitable for reacting with hydroxide anions. Hence, the BG dye molecules become unstable at higher pH 11 value.[59,60] Therefore, we

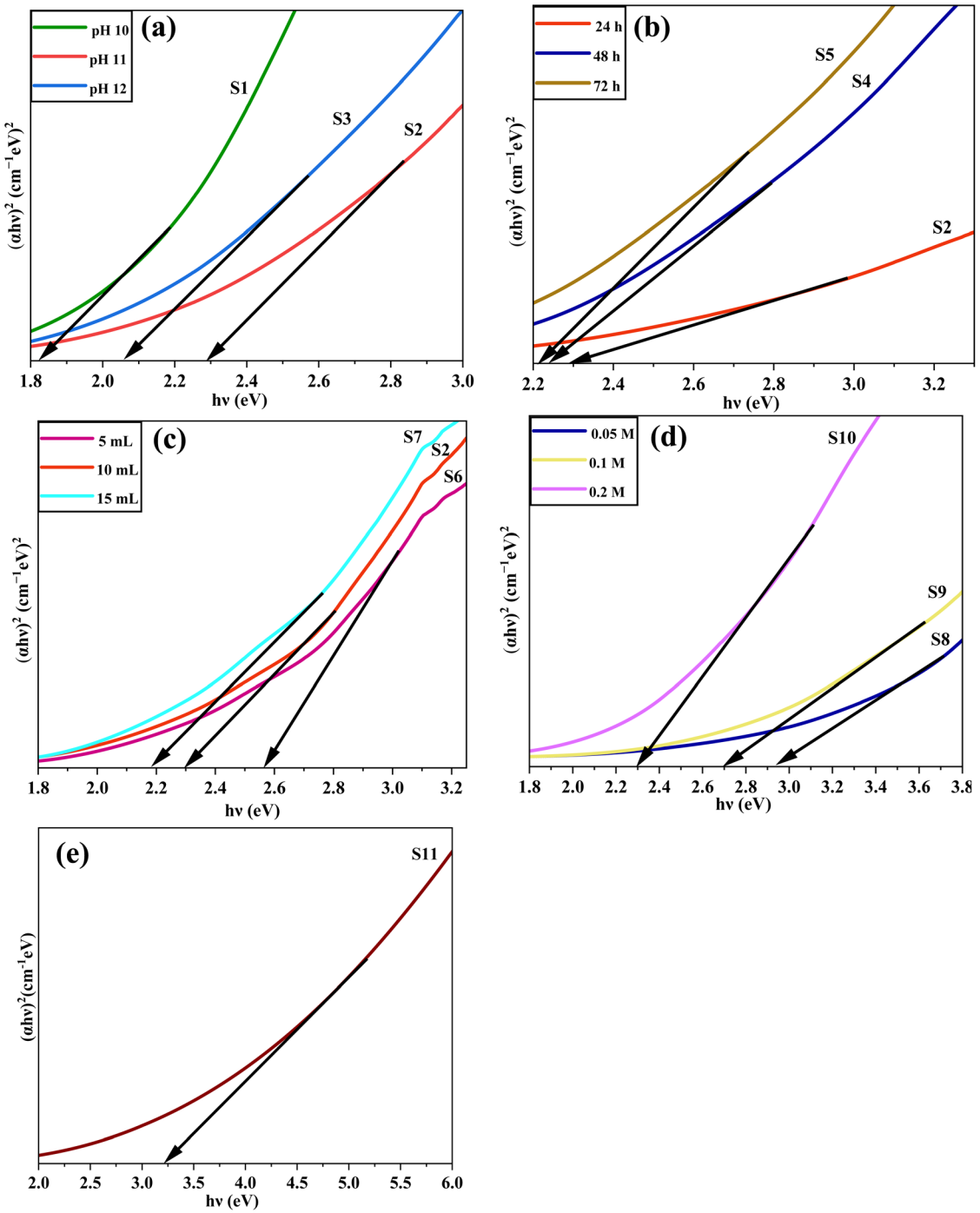

Fig. 4 (a) Effect of pH of the solution (S1 – pH 10, S2 – pH 11, S3 – pH 12), (b) effect of reaction time (S2 – 24 h, S4 – 48 h, S5 – 72 h), (c) effect of the volume of algal extract (S6 – 5 mL, S2 – 10 mL, S7 – 15 mL), and (d) effect of copper ions concentration (S8 – 0.05 M, S9 – 0.1 M, S10 – 0.2 M) on the band gap value of biosynthesized CuO NPs using Tauc plot; (e) Tauc plot of chemically synthesized CuO NPs (S11).

have selected pH 9 to optimize other parameters for the BG dye degradation.

A similar effect of pH was observed with the MG dye (Fig. S5d†). The photodegradation rate was enhanced from 48.88% to 84.32% by varying the pH from 3 to 9. The 97.99% degradation was observed with pH 11 within 1 min due to the instability of the dye at a higher pH value. Both BG and MG dyes possess cationic nature. In an alkaline medium, the large concentration of OH^- ions lead to a negative charge on the catalyst surface. This increases the electrostatic attraction between the negatively charged catalyst surface and cationic dye molecules, resulting in enhanced adsorption of the dye molecules on the catalyst surface.[61] Consequently, the degradation rate of the BG and MG dyes was increased at higher pH values.

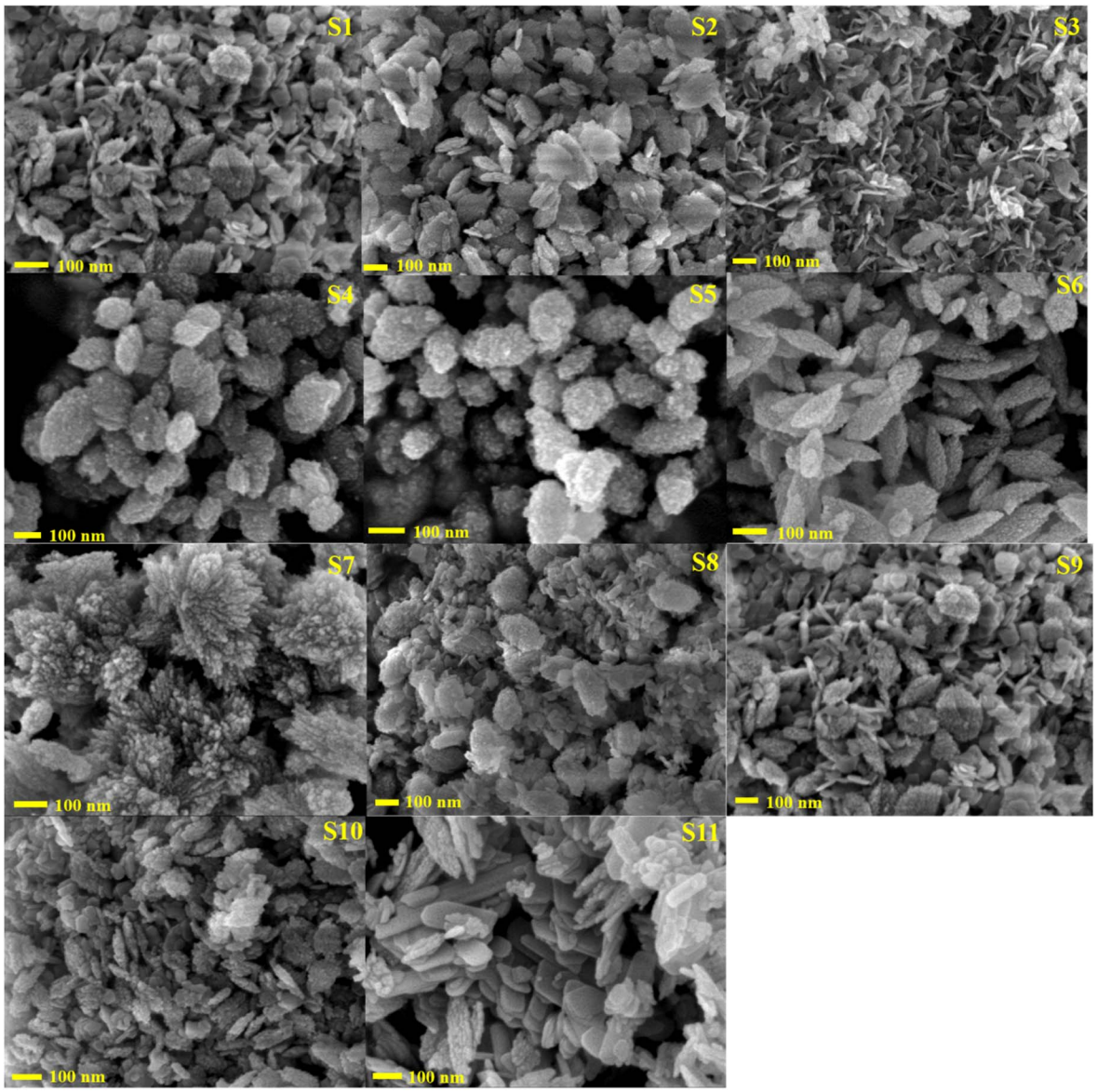

Fig. 5 FE-SEM image of the biosynthesized CuO NPs (S1–S10) and chemically synthesized CuO NPs (S11).

Conversely, in an acidic medium, the excess of H^+ ions result in a positive charge on the catalyst surface. This positively charged catalyst surface repels cationic dye molecules and decreases the adsorption process. Hence, at lower pH values, the degradation rate of the BG and MG dyes was reduced.[60]

Fig. S5c† demonstrates the degradation rate of EBT dye on CuO NPs through photocatalysis at various pH values. Results showed that at pH values of 3, 5, 7, 9, and 11, the degradation rates were 50.47%, 58.68%, 71.28%, 80.07%, and 83.81%, respectively. The photocatalytic degradation of the dye was found to decrease in an acidic environment compared to neutral pH conditions, whereas the degradation rate increased in a basic environment. The highest rate of degradation was observed at pH 11. A similar result of the effect of pH on EBT dye dilapidation was observed by Lanjwani *et al.*[11] In the basic medium, the concentration of OH^- ions increased. An increase in the concentration of hydroxyl ions results in a corresponding increase in the concentration of hydroxyl radicals ($^{\bullet}OH$).[62] The increase in hydroxyl radicals ($^{\bullet}OH$) results in a higher rate of photocatalytic degradation of EBT dye.

From the findings, we can infer that the optimized pH values for the photodegradation of BBY, BG, EBT, and MG dyes using biosynthesized CuO NPs were 3, 9, 11, and 9, respectively.

Effect of catalyst dosage. In this study, the effect of catalyst dosage on the degradation of four different dyes, namely BBY, BG, EBT, and MG, was investigated (Fig. S6†). The concentration of dye was kept constant at 75 ppm, and the pH value that was optimized earlier was utilized for each dye. For BBY dye, the optimized pH value was 3, while for BG and MG dyes, the pH value was set to 9, and for EBT dye, the pH value was 11. A series of experiments were performed by varying the dosage, 0.01 g, 0.03 g, 0.05 g, 0.07 g, and 0.09 g, of CuO NPs.

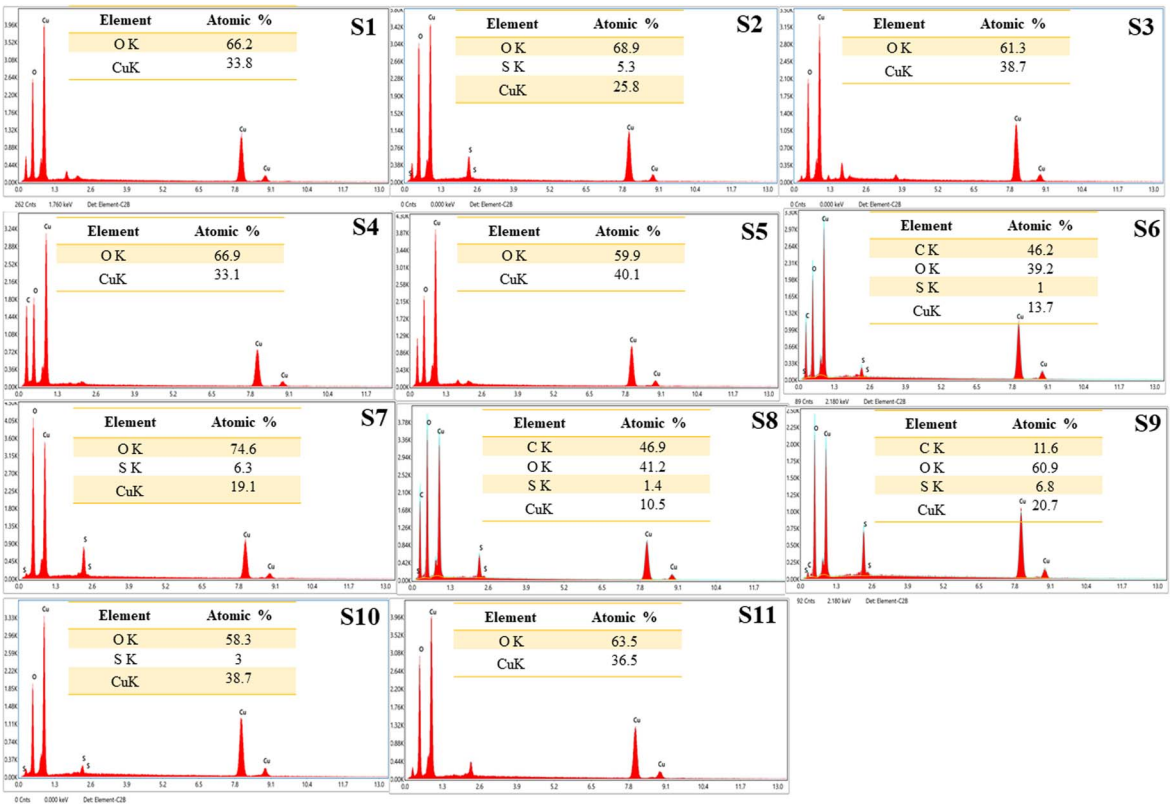

Fig. 6 EDS spectra of the biosynthesized CuO NPs (S1–S10) and chemically synthesized CuO NPs (S11).

The results showed that the degradation percentage of BBY dye increased up to 0.05 g of the catalyst and then decreased with a further increase in catalyst loading up to 0.09 g (Fig.-S6a†). The maximum degradation of 87.37% was observed at 0.05 g catalyst loading.

On the other hand, the observed degradation rate of BG dye with 0.01, 0.03, 0.05, 0.07, and 0.09 g catalyst loading were 88.28%, 93.04%, 95.72%, 96.92%, and 81.93% after 60 min, respectively (Fig. S6b†). The results demonstrated that the degradation rate was enhanced with an increase in the catalyst loading from 0.01 g to 0.07 g after a further increase in the catalyst loading decreased the degradation efficacy. The optimized CuO NPs catalyst dosage for BG dye was found to be 0.07 g.

For EBT dye, an increment in the degradation efficiency was observed up to optimal catalyst dosage; after that, subsequent increment in the dosage of the catalyst reduced the percentage of dye degradation (Fig. S6c†). The degradation rate increased from 51.46% to 85.84%, with an increase in catalyst loading from 0.01 g to 0.05 g after 90 min of light illumination. The maximum degradation efficiency of 85.84% was achieved at 0.05 g catalyst loading, followed by a decreased degradation rate of 80.56% at 0.09 g catalyst loading.

For MG dye, the optimized catalyst dosage was found to be 0.03 g (Fig. S6d†). The degradation rate increased from 93.04% to 95.72%, with an increase in catalyst dosage from 0.01 g to 0.03 g, afterwards a decrease in degradation efficiency was observed. The degradation rate was reduced to 81.92% at 0.09 g catalyst loading.

Based on the findings, it can be inferred that the optimal catalyst dosage for the BBY, BG, EBT, and MG dyes degradation was 0.05 g, 0.07 g, 0.05 g, and 0.03 g, respectively. The upgradation in the degradation efficacy up to a particular value of the catalyst loading was mainly ascribed to more numbers of available active sites. Nevertheless, after an optimum dosage, a decrease in the degradation rate was observed due to the turbidity of the solution with more catalyst particles or the aggregation of the catalyst. Because of the aggregation of the catalyst particles, a smaller number of active sites were available for the degradation of the dye on the surface of the catalyst, which reduced the efficacy of the CuO NPs to degrade the dyes.

Effect of initial dye concentration. The photodegradation process is significantly influenced by the initial concentration of the dye. The potency of CuO NPs for the degradation of BBY, BG, EBT, and MG dyes was investigated at different initial dye concentrations (50 ppm, 62.50 ppm, 75 ppm, 87.50 ppm, and 100 ppm) under visible light radiations (Fig. 7). The other parameters, pH and catalyst dosage, were kept constant.

The degradation of BBY dye was studied at different initial concentrations (50–100 ppm) over a period of 120 min (Fig. 7a). The degradation rate increased with increasing initial dye concentration from 50 ppm to 87.50 ppm, reaching a maximum of 95.78% degradation at 87.50 ppm of initial dye

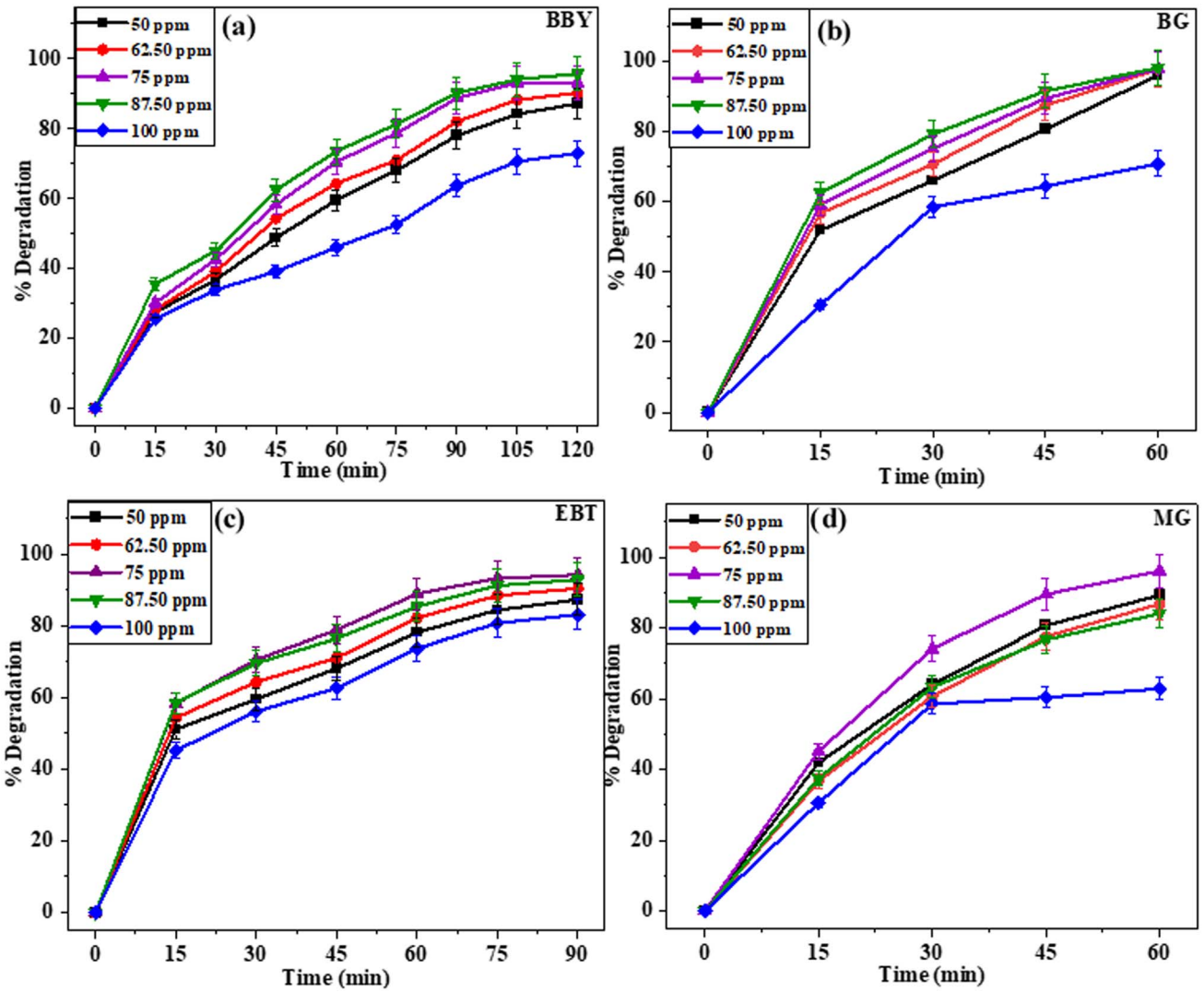

Fig. 7 The effect of initial dye concentration on the degradation percentage of dyes: (a) BBY, (b) BG, (c) EBT, and (d) MG using biosynthesized CuO NPs (S8).

concentration. However, at the highest concentration of 100 ppm, the degradation rate decreased to 73.03%.

The degradation rate of BG dye was observed to be 96.05%, 97.72%, 97.89%, 98.02%, and 70.80% for initial dye concentrations of 50, 62.50, 75, 87.50, and 100 ppm, respectively, after 60 min (Fig. 7b). Similar to the BBY dye results, the highest degradation rate was observed at an initial BG dye concentration of 87.50 ppm, which resulted in a degradation rate of 98.02%. However, the degradation rate decreased significantly to 70.80% at the highest concentration of 100 ppm.

The degradation rate of EBT dye with 50, 62.50, 75, 87.50, and 100 ppm initial dye concentrations was 87.25%, 90.34%, 94.15%, 92.78%, and 83.03% after 90 min (Fig. 7c). The highest degradation rate was observed at an initial EBT dye concentration of 75 ppm, which resulted in 94.15% degradation.

The degradation rate of MG dye was found to be 89.20%, 86.72%, 96.04%, 84.02%, and 62.80% for initial dye concentrations of 50, 62.50, 75, 87.50, and 100 ppm, respectively, after 60 min of light radiation (Fig. 7d). The maximum rate of dilapidation was seen at an initial dye concentration of 75 ppm. Although, at the highest concentration of 100 ppm, the degradation rate was reduced significantly to 62.80%.

The observed behaviour of dependence of photocatalytic degradation rate on the initial dye concentration can be attributed to the fact that a higher initial concentration of the dye may lead to the saturation of active sites on the surface of the nanoparticles, thereby hindering the degradation process. In addition to this, as the concentration of the dye was increased, the colour of solution became more intense, thereby impeding the penetration of light to the catalyst surface. These outcomes suggest that the initial dye concentration is a crucial factor in determining the photodegradation efficiency of dyes.

Kinetics of photodegradation. The kinetic study of the photodegradation rate was investigated at the optimized reaction parameters. Fig. 8 illustrates the kinetic plot of $\ln(C_0/C_t)$ *versus* time (min). Based on the results of the kinetics analysis, it is clear that the data exhibit a strong fit to the pseudo-first-order kinetic model and adhere to its principles for all four dyes.

The calculated kinetic rate constant (k) and R^2 values are represented in Table 8 at optimized reaction conditions for all the selected dyes. The kinetic rate constant (k) for the BBY, BG, EBT, and MG dyes was 0.02610 min^{-1}, 0.06254 min^{-1}, 0.03209 min^{-1}, and 0.05456 min^{-1}, respectively (Fig. 9). The results indicate that CuO NPs exhibit the highest rate constant value for the BG dye dilapidation.

Reusability of the CuO NPs. To ensure the practical applicability of the catalyst, it is essential to evaluate its photostability and reusability. In this regard, the CuO NPs were subjected to photocatalytic degradation experiments of selected dyes for five cyclic runs under the illumination of visible light, and the results are illustrated in Fig. 10. At the end of each experimental cycle, the photocatalyst was collected using centrifugation and washed with DI to reuse in subsequent cycles. The photodegradation efficacy of the CuO NPs for BBY, BG, EBT, and MG dyes was decreased by 13.22%, 4.62%, 14.19%, and 15.15%, respectively, after five consecutive cycles. Among the four dyes, the BG dye exhibited the highest reusability of the CuO NPs for the photodegradation and only a 4.62% reduction in degradation efficiency was observed after five degradation cycles. Despite the reduction in efficiency, the catalyst continued to exhibit excellent performance, proving a promising candidate for wastewater treatment that requires a reliable and sustainable photocatalyst. The observed decrease in photocatalytic activity of the catalyst after multiple cycles can be attributed to two factors: firstly, the loss of photocatalyst during the process of recollection could have led to a decrease in the amount of active catalyst, resulting in a decrement in the efficiency; secondly, the deposition of intermediate species (formed during the dye degradation process) on the active sites during the dye degradation process could have also contributed to a decrease in the photocatalytic activity of the catalyst.[63]

Scavenging activity. To determine the relative contribution of primary reactive species in the photocatalytic degradation process, a series of scavenging experiments were conducted. During the experiments, scavenging reagents, potassium dichromate ($K_2Cr_2O_7$) for electrons (e−), disodium EDTA for holes (h^+), 2-propanol (IPA) for hydroxyl radicals ($^{\bullet}OH$), and benzoquinone (BQ) for superoxide anion radicals ($O_2^{\bullet-}$), were chosen to selectively scavenge specific primary reactive species.

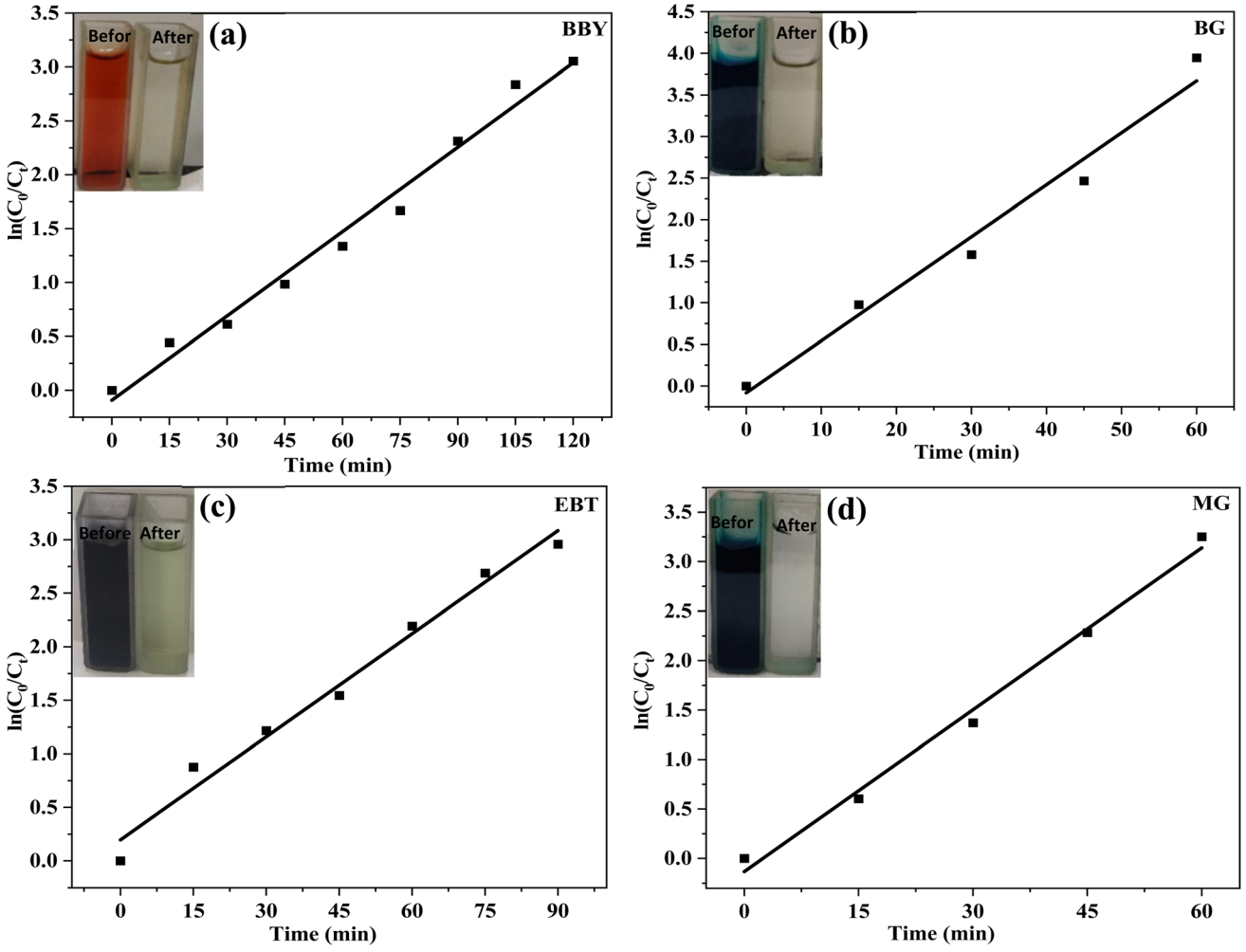

Fig. 8 Pseudo-first-order kinetics plots of the photodegradation of dyes: (a) BBY, (b) BG, (c) EBT, and (d) MG. The inset images depict the colour of the dye solution before and after the degradation process.

Table 8 Rate constant (k), and R^2 at optimized reaction conditions for the degradation of the BBY, BG, EBT, and MG dyes using CuO NPs (S8)

S. no.	Dye	pH	Catalyst dosage	Initial concentration of dye	Degradation time (min)	% degradation	Rate constant (k) (min^{-1})	R^2
1	BBY	3	0.05 g	87.50 ppm	120	95.78%	0.0261	0.98484
2	BG	9	0.07 g	87.50 ppm	60	98.02%	0.06254	0.97635
3	EBT	9	0.05 g	75 ppm	90	94.15%	0.03209	0.98195
4	MG	11	0.03 g	75 ppm	60	96.04%	0.05456	0.99175

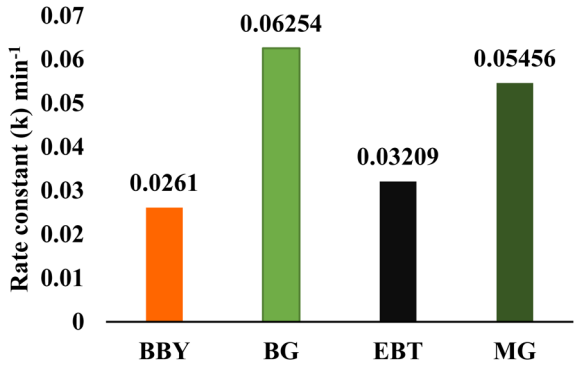

Fig. 9 Kinetic rate constant values for photodegradation of BBY, BG, EBT, and MG dyes by biosynthesized CuO NPs (S8) at optimized reaction conditions.

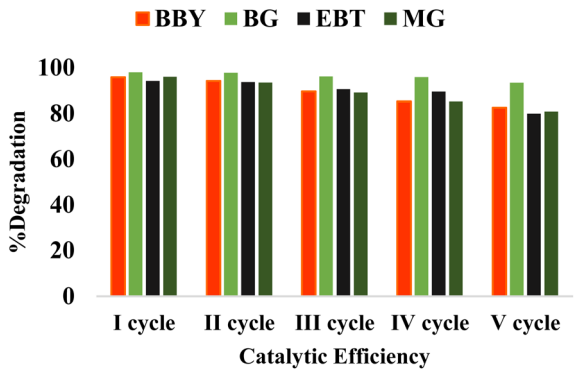

Fig. 10 Reusability of the biosynthesized CuO NPs (S8) for the photodegradation of the BBY, BG, EBT, and MG dyes.

The scavenging experiment helps to understand the contribution of these reactive species in the photodegradation process.

The degradation efficiency of BBY, BG, EBT, and MG dyes was significantly affected by the addition of IPA and BQ scavengers, as evidenced by the substantial reduction in the percentage degradation (Fig. 11). The degradation rate was reduced to 35.41%, 50.87%, 64.91%, and 28.49% for BBY, BG, EBT, and MG dyes, respectively, by IPA scavenger. Similarly, the addition of a BQ scavenger also diminished the degradation rate to 46.85%, 58.67%, 38.96%, and 49.76% for BBY, BG, EBT, and MG dyes, respectively. The degradation of all dyes was reduced in the presence of IPA and BQ, indicating that hydroxyl radicals ($^{\bullet}OH$) and superoxide anion radicals ($O_2^{\bullet-}$) were the major contributors to the degradation of dyes. Whereas EDTA and $K_2Cr_2O_7$ did not significantly affect the photodegradation process of all four dyes. These results suggest that the primary contributors to dye degradation were hydroxyl radicals ($^{\bullet}OH$) and superoxide anion radicals ($O_2^{\bullet-}$). The electrons (e^-) and holes (h^+) were not directly involved in the degradation process, instead played a role in the formation of the hydroxyl radicals ($^{\bullet}OH$) and superoxide anion radicals ($O_2^{\bullet-}$).

A plausible mechanism for the photodegradation. Based on the outcomes of the scavenging experiments and the values of band edge potential, a plausible mechanism for the photocatalytic degradation of selected dyes using the biosynthesized CuO NPs as a photocatalyst is proposed. The band gap value of the CuO NPs (S8) selected for the photocatalytic degradation of the dyes was 2.93 eV, as calculated by Tauc plot. The edge potential values for the valence band (E_{VB}) and conduction band (E_{CB}) edges were calculated using eqn (5) and (6).

$$E_{CB} = \chi(A_aB_b) - 0.5E_g + E_e \quad (5)$$

$$E_{VB} = E_{CB} + E_g \quad (6)$$

$$\chi(A_aB_b) = [\chi(A)^a \cdot \chi(B)^b]^{1/(a+b)} \quad (7)$$

The E_g refers to the band gap of the CuO NPs (S8), which is 2.93 eV. E_e represents the energy of a free electron on the Normal Hydrogen Electrode (NHE) scale, which is −4.50 eV.[63] To calculate $\chi(A_aB_b)$, eqn (7) is used, which demonstrates the geometric mean of the electronegativity values of the constituent atoms, *i.e.*, copper (Cu) and oxygen (O).[64] The electronegativity of copper (Cu) and oxygen (O) are 4.48 eV and 7.54 eV, respectively.[65] The calculated band edge potential of the valence band (E_{VB}) and conduction band (E_{CB}) was 2.775 eV and −0.155 eV, respectively.

The proposed mechanism of dye dilapidation is schematically illustrated in Fig. 12. Under exposure of visible light, the CuO NPs photocatalyst undergoes a process of electron (e^-) excitation from the valence band (VB) to the conduction band (CB). Due to this process, positively charged holes (h^+) were generated in the VB and electrons (e^-) in the CB. The generated electrons react with the adsorbed oxygen molecules (O_2) on the surface of the photocatalyst, producing superoxide anion radicals ($O_2^{\bullet-}$), while the holes in the VB oxidize water to form free hydroxyl radicals ($^{\bullet}OH$). The free radicals produced during the process further initiate a series of reactions, eventually resulting in the degradation of organic dyes. Additionally, the metabolites of algae capped on the CuO NPs enhance the adsorption of dye molecules on the photocatalyst surface. The plausible reactions incorporated in the

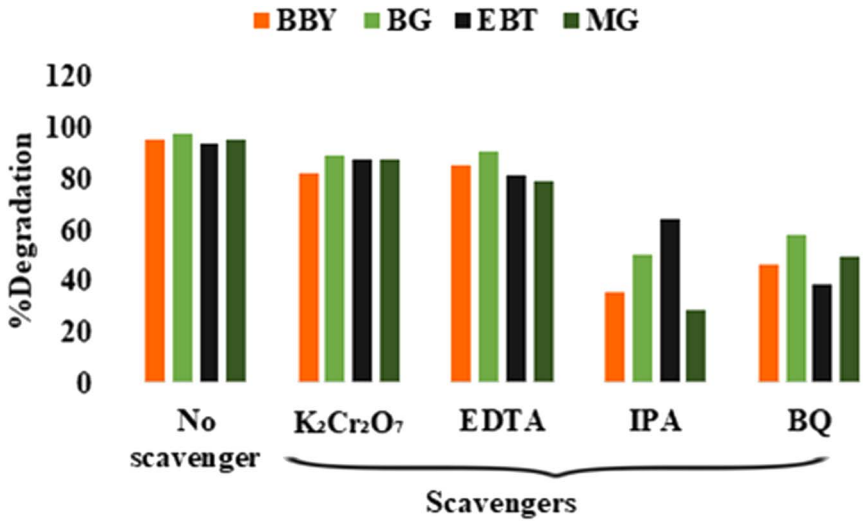

Fig. 11 The effect of different scavengers on the degradation rate of BBY, BG, EBT, and MG dyes.

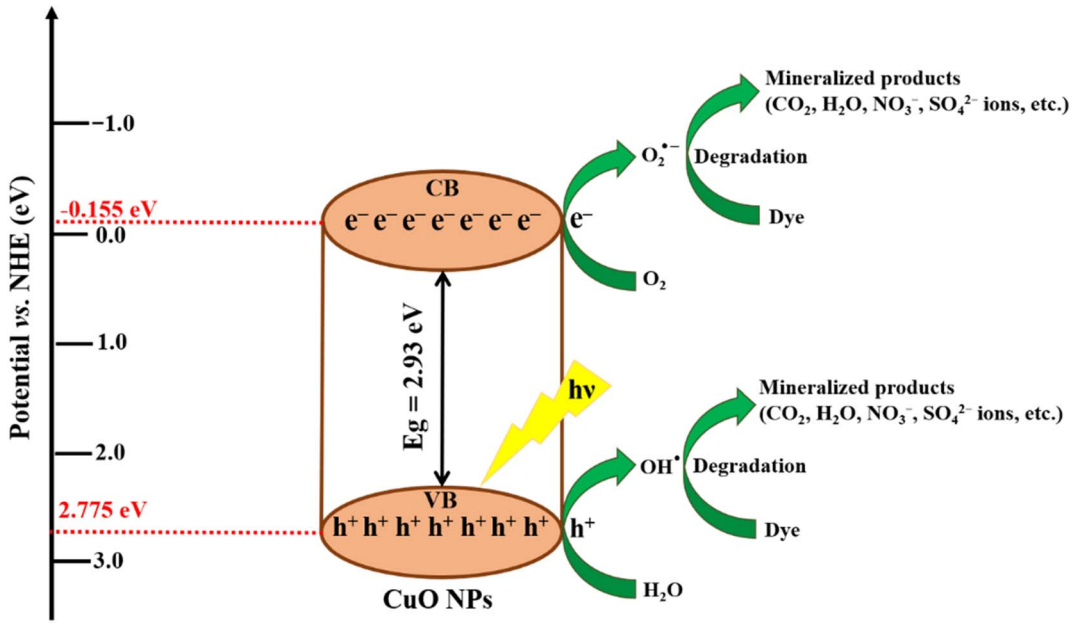

Fig. 12 A plausible mechanism of degradation of dyes (BBY, BG, EBY, and MG) by biosynthesized CuO NPs (S8).

photodegradation of dyes (BBY, BG, EBT, and MG dye) using the CuO NPs are revealed by eqn (8)–(16).

$$^{1}\mathrm{Dye}_0 \xrightarrow{h\nu} {}^{1}\mathrm{Dye}_1 \quad (8)$$

$$^{1}\mathrm{Dye}_1 \xrightarrow{\mathrm{ISC}} {}^{3}\mathrm{Dye}_1 \quad (9)$$

$$\mathrm{CuO} \xrightarrow{h\nu} \mathrm{CuO}\left(h_{VB}^{+} + e_{CB}^{-}\right) \quad (10)$$

$$h_{VB}{}^{+} + H_2O \rightarrow {}^{\bullet}OH + H^{+} \quad (11)$$

$$O_2 + e_{CB}{}^{-} \rightarrow O_2{}^{\bullet -} \text{ (dissolved oxygen)} \quad (12)$$

$${}^{\bullet}OH + {}^{3}\mathrm{Dye}_1 \rightarrow {}^{3}\mathrm{Dye}_1 \text{ (Leuco unstable form)} \quad (13)$$

$$O_2{}^{\bullet -} + {}^{3}\mathrm{Dye}_1 \rightarrow {}^{3}\mathrm{Dye}_1 \text{ (Leuco unstable form)} \quad (14)$$

$$^{3}\mathrm{Dye}_1 \text{ (Leuco)} \xrightarrow{{}^{\bullet}OH} \text{mineralized products } (CO_2, H_2O, NO_3{}^{-}, SO_4{}^{-} \text{ ions, } etc.) \quad (15)$$

$$^{3}\mathrm{Dye} \text{ (Leuco)} \xrightarrow{O_2{}^{\bullet -}} \text{mineralized products } (CO_2, H_2O, NO_3{}^{-}, SO_4{}^{2-} \text{ ions, } etc.) \quad (16)$$

Conclusions

The proposed strategy for the green synthesis of CuO NPs using an *Asterarcys quadricellulare* algal extract includes a novel, simple, and eco-friendly approach. The study of various

reaction parameters for the biosynthesis of CuO NPs disclosed that changing the pH, time, volume of algal extract, and concentration of copper ions, provided the different shapes and sizes of the synthesized CuO NPs. The best results were obtained with the reaction condition, pH 11, 24 h time, 5 mL volume of algal extract, and 0.05 M concentration of the copper ions. The minute change in the reaction conditions provided the desirable change in the crystallite size, band gap value, and shape of the synthesized CuO NPs. The biosynthesized CuO NPs demonstrate excellent degradation efficiency for BBY, BG, EBT, and MG dyes, under visible light radiations. The degradation of dyes continued after five consecutive cycles showing higher stability and reusability of the CuO NPs catalyst. Therefore, biosynthesized CuO NPs can be effectively used for the degradation of dyes and helps in the wastewater treatment process. Owing to the environmental benefits of algal-mediated CuO NPs, further research utilizing these nanoparticles for antibacterial activity are in progress in our laboratory.

Author contributions

Manisha Khandelwal: investigation, visualization, data curation, formal analysis, methodology, writing – original draft. Sunita Choudhary: formal analysis, data curation. Harish: software, resources, validation. Ashok Kumawat: data curation, formal analysis. Kamakhya Prakash Misra: formal analysis, resources, validation, writing-review & editing. Devendra Singh Rathore: software, resources, validation. Rama Kanwar Khangarot: conceptualization, visualization, methodology, resources, supervision, validation, writing-review & editing.

Conflicts of interest

There are no conflicts to declare.

Acknowledgements

The authors are grateful to the Department of Chemistry, Mohanlal Sukhadia University, Udaipur (Raj.), India, for providing the necessary laboratory facilities. The authors thank the Department of Physics, Department of Botany, and Department of Environmental Sciences, Mohanlal Sukhadia University, Udaipur, for providing the XRD facility, algal culture, and UV-vis spectrophotometer, respectively. The authors acknowledge the facilities of Manipal University Jaipur (MUJ), India, for UV-vis, FTIR, and FE-SEM coupled with EDS. RKK and MK thank University Grants Commission, New Delhi, India, for UGC-Start-Up Project [No. F. 30-476/2019 (BSR)] and Fellowship [115/CSIRNETJUNE2019], respectively, for providing financial support to conduct the research work. DSR thanks the Science and Engineering Research Board, Department of Science and Technology (DST), New Delhi, for a core research grant (CRG/2019/006919).

References

1 R. H. Waghchaure, V. A. Adole and B. S. Jagdale, *Inorg. Chem. Commun.*, 2022, 109764.
2 H. He, Z. Luo and C. Yu, *J. Photochem. Photobiol., A*, 2020, **401**, 112735.
3 R. Al-Tohamy, S. S. Ali, F. Li, K. M. Okasha, Y. A.-G. Mahmoud, T. Elsamahy, H. Jiao, Y. Fu and J. Sun, *Ecotoxicol. Environ. Saf.*, 2022, **231**, 113160.
4 J. Essomba, J. Alla, P. Belibi and N. Fathima, *Int. J. Environ. Sci. Technol.*, 2022, **19**, 5181–5194.
5 H. A. Hamad, S. AbdElhafez, M. Elsenety, M. K. Sorour, N. Amin, O. Abdelwahab and E. Z. El-Ashtoukhy, *Fuel*, 2022, **323**, 124288.
6 M. M. Silva, F. H. Reboredo and F. C. Lidon, *Foods*, 2022, **11**, 379.
7 M. Khandelwal, D. Sharma, G. Pemawat and R. K. Khangarot, in *Current and Future Perspectives of Environmental Pollution and its Remediation*, Thanuj International Publishers, Tamil Nadu, 2022, vol. 1, pp. 36–49.
8 S. Begum, S. R. Mishra and M. Ahmaruzzaman, *Inorg. Chem. Commun.*, 2022, **143**, 109721.
9 M. Bhaumik, A. Maity and H. G. Brink, *J. Colloid Interface Sci.*, 2022, **611**, 408–420.
10 K. Selvam, C. Sudhakar, T. Selvankumar, B. Senthilkumar, W. Kim, M. M. Al-Ansari and L. Al-Humaid, *Appl. Nanosci.*, 2023, **13**, 2837–2843.
11 M. F. Lanjwani, M. Y. Khuhawar, T. M. J. Khuhawar, A. H. Lanjwani, S. Q. Memon, W. A. Soomro and I. K. Rind, *J. Cluster Sci.*, 2022, 1–12.
12 B. Pandey, P. Singh and V. Kumar, *Environ. Nanotechnol., Monit. Manage.*, 2021, **16**, 100596.
13 G. Bal and A. Thakur, *Mater. Today: Proc.*, 2022, **50**, 1575–1579.
14 H. He, Z. Luo, Z.-Y. Tang and C. Yu, *Appl. Surf. Sci.*, 2019, **490**, 460–468.
15 H. He, Z. Luo and C. Yu, *Colloids Surf., A*, 2021, **613**, 126099.
16 Z. Masood, A. Ikhlaq, A. Akram, U. Y. Qazi, O. S. Rizvi, R. Javaid, A. Alazmi, M. Madkour and F. Qi, *Catalysts*, 2022, **12**, 741.
17 R. K. Singh, S. S. Behera, K. R. Singh, S. Mishra, B. Panigrahi, T. R. Sahoo, P. K. Parhi and D. Mandal, *J. Photochem. Photobiol., A*, 2020, **400**, 112704.
18 K. Mahmood, U. Amara, S. Siddique, M. Usman, Q. Peng, M. Khalid, A. Hussain, M. Ajmal, A. Ahmad and S. H. Sumrra, *J. Nanostruct. Chem.*, 2022, **12**, 329–341.
19 H. Naeem, H. M. Tofil, M. Soliman, A. Hai, S. H. H. Zaidi, N. Kizilbash, D. Alruwaili, M. Ajmal and M. Siddiq, *Molecules*, 2023, **28**, 926.
20 K. Saeed, I. Khan, T. Gul and M. Sadiq, *Appl. Water Sci.*, 2017, **7**, 3841–3848.
21 K. Khalid, A. Zahra, U. Amara, M. Khalid, M. Hanif, M. Aziz, K. Mahmood, M. Ajmal, M. Asif and K. Saeed, *Chemosphere*, 2023, **338**, 139531.
22 R. K. Khangarot, M. Khandelwal and R. Singh, in *Metal Nanocomposites for Energy and Environmental Applications*, Springer, 2022, pp. 489–508.
23 H. He, J. Xiao, Z. Liu, B. Yang, D. Wang, X. Peng, L. Zeng, Z. Li, L. Lei, M. Qiu and Y. Hou, *Chem. Eng. J.*, 2023, **453**, 139751.

24 M. Khandelwal, A. Kumawat, K. P. Misra and R. K. Khangarot, *Part. Sci. Technol.*, 2022, **41**, 640–652.
25 T. Naseem and T. Durrani, *Environ. Chem. Ecotoxicol.*, 2021, **3**, 59–75.
26 H. N. Cuong, S. Pansambal, S. Ghotekar, R. Oza, N. T. Thanh Hai, N. M. Viet and V.-H. Nguyen, *Environ. Res.*, 2022, **203**, 111858.
27 S. Yadav, A. Jain and P. Malhotra, *Green Chem.*, 2019, **21**, 937–955.
28 S. S. Chan, S. S. Low, K. W. Chew, T. C. Ling, J. Rinklebe, J. C. Juan, E. P. Ng and P. L. Show, *Environ. Res.*, 2022, **212**, 113140.
29 A. Mukherjee, D. Sarkar and S. Sasmal, *Front. Microbiol.*, 2021, **12**, 693899.
30 Y. Abboud, T. Saffaj, A. Chagraoui, A. El Bouari, K. Brouzi, O. Tanane and B. Ihssane, *Appl. Nanosci.*, 2014, **4**, 571–576.
31 S. V. P. Ramaswamy, S. Narendhran and R. Sivaraj, *Bull. Mater. Sci.*, 2016, **39**, 361–364.
32 H. Gu, X. Chen, F. Chen, X. Zhou and Z. Parsaee, *Ultrason. Sonochem.*, 2018, **41**, 109–119.
33 P. Bhattacharya, S. Swarnakar, S. Ghosh, S. Majumdar and S. Banerjee, *J. Environ. Chem. Eng.*, 2019, **7**, 102867.
34 K. Araya-Castro, T.-C. Chao, B. Durán-Vinet, C. Cisternas, G. Ciudad and O. Rubilar, *Processes*, 2020, **9**, 78.
35 S. Rajeshkumar, N. T. Nandhini, K. Manjunath, P. Sivaperumal, G. Krishna Prasad, S. S. Alotaibi and S. M. Roopan, *J. Mol. Struct.*, 2021, **1242**, 130724.
36 N. Ain, N. Safdar and A. Yasmin, *Colloids Surf., B*, 2019, **178**, 66–73.
37 D. Letchumanan, S. P. Sok, S. Ibrahim, N. H. Nagoor and N. M. Arshad, *Biomolecules*, 2021, **11**, 564.
38 H. Veisi, B. Karmakar, T. Tamoradi, S. Hemmati, M. Hekmati and M. Hamelian, *Sci. Rep.*, 2021, **11**, 1983.
39 S. Asbrink and A. Waskowska, *J. Phys.: Condens. Matter*, 1991, **3**, 8173.
40 A. Sharma, R. Khangarot, K. P. Misra, D. Misra, S. Chattopadhyay, P. D. Babu and N. Halder, *Phys. Scr.*, 2021, 075803.
41 A. Sharma, R. K. Khangarot, N. Kumar, S. Chattopadhyay and K. P. Misra, *Mater. Technol.*, 2021, **36**, 541–551.
42 A. Sharma, A. Kumawat, B. Raput, R. K. Khangarot, U. Valiyaneerilakkal, S. Chattopadhyay and K. P. Misra, *Effect of Heavy Al Doping on Microstructural and Morphological Behavior of ZnO Thin Film Deposited by Sol-Gel Spin Coating*, AIP Publishing LLC, 2021, vol. 2352, p. 040001.
43 A. Arya, V. Mishra and T. S. Chundawat, *Chem. Data Collect.*, 2019, **20**, 100190.
44 S. Tharani, D. Bharathi and R. Ranjithkumar, *Biocatal. Agric. Biotechnol.*, 2020, **30**, 101838.
45 M. Forouzandeh-Malati, F. Ganjali, E. Zamiri, S. Zarei-Shokat, F. Jalali, M. Padervand, R. Taheri-Ledari and A. Maleki, *Langmuir*, 2022, **38**, 13728–13743.
46 K. S. Prasad, H. Patel, T. Patel, K. Patel and K. Selvaraj, *Colloids Surf., B*, 2013, **103**, 261–266.
47 S. Shende, A. Gade and M. Rai, *Environ. Chem. Lett.*, 2017, **15**, 427–434.
48 A. Arya, K. Gupta, T. S. Chundawat and D. Vaya, *Bioinorg. Chem. Appl.*, 2018, **2018**, 7879403.
49 B. Sharma, D. D. Purkayastha, S. Hazra, L. Gogoi, C. R. Bhattacharjee, N. N. Ghosh and J. Rout, *Mater. Lett.*, 2014, **116**, 94–97.
50 C. Adina, F. Florinela, T. Abdelmoumen and S. Carmen, *Rom. Biotechnol. Lett.*, 2010, **15**, 5738–5744.
51 S. Vasantharaj, S. Sathiyavimal, M. Saravanan, P. Senthilkumar, K. Gnanasekaran, M. Shanmugavel, E. Manikandan and A. Pugazhendhi, *J. Photochem. Photobiol., B*, 2019, **191**, 143–149.
52 M. Bilal, M. Ikram, T. Shujah, A. Haider, S. Naz, A. Ul-Hamid, M. Naz, J. Haider, I. Shahzadi and W. Nabgan, *ACS Omega*, 2022, **7**, 41614–41626.
53 K. M. Navada, G. Nagaraja, J. N. D'Souza, S. Kouser, R. Ranjitha and D. Manasa, *Appl. Nanosci.*, 2020, **10**, 4221–4240.
54 A. Sharma, A. Kumawat, S. Chattopadhyay, R. K. Khangarot, N. Halder, R. Misra and K. P. Misra, *Mater. Today: Proc.*, 2022, **60**, 21–25.
55 A. Sharma, A. Kumawat, S. Chattopadhyay, R. K. Khangarot, R. Misra and K. P. Misra, *Mater. Technol.*, 2021, 1–10.
56 S. Bose, B. K. Tripathy, A. Debnath and M. Kumar, *Ultrason. Sonochem.*, 2021, **75**, 105592.
57 Y. M. Hunge, A. A. Yadav and S.-W. Kang, *Catalysts*, 2022, **12**, 1290.
58 K. D. Sirdeshpande, A. Sridhar, K. M. Cholkar and R. Selvaraj, *Appl. Nanosci.*, 2018, **8**, 675–683.
59 S. Kaur, S. Sharma, A. Umar, S. Singh, S. Mehta and S. K. Kansal, *Superlattices Microstruct.*, 2017, **103**, 365–375.
60 T. B. Mbuyazi and P. A. Ajibade, *Results Mater.*, 2022, **16**, 100328.
61 P. Muhambihai, V. Rama and P. Subramaniam, *Environ. Nanotechnol., Monit. Manage.*, 2020, **14**, 100360.
62 M. Karimi-Shamsabadi, M. Behpour, A. K. Babaheidari and Z. Saberi, *J. Photochem. Photobiol., A*, 2017, **346**, 133–143.
63 P. L. Meena, K. Poswal, A. K. Surela and J. K. Saini, *Adv. Compos. Hybrid Mater.*, 2023, **6**, 16.
64 M. Mousavi, A. Habibi-Yangjeh and M. Abitorabi, *J. Colloid Interface Sci.*, 2016, **480**, 218–231.
65 R. G. Pearson, *Inorg. Chem.*, 1988, **27**, 734–740.